Morphology-Tunable Synthesis of Intrinsic Room-Temperature Ferromagnetic γ-Fe2O3 Nanoflakes

Jia, Z.; Wang, W.; Li, Z.; Sun, R.; Zhou, S.; Leonard Deepak, F.; Su, C.; Li, Y.; Wang, Z.;

Originally published:

May 2021

ACS Applied Materials and Interfaces 13(2021)20, 24051-24061

DOI: https://doi.org/10.1021/acsami.1c05342

Morphology Tunable Synthesis of Intrinsic Room-Temperature Ferromagnetic γ-Fe_2O_3 Nanoflakes

Zhiyan Jia,[1,2] Zichao Li,[3,] Rong Sun,[2] Chenliang Su,[1] Shengqiang Zhou,[3] Francis Leonard Deepak,[2] Ying Li,[1,2,*] Wenjie Wang,[4,*] and Zhongchang Wang[1,2,*]

[1]International Collaborative Laboratory of 2D Materials for Optoelectronic Science and Technology of Ministry of Education, Engineering Technology Research Center for 2D Materials Information Functional Devices and Systems of Guangdong Province, Institute of Microscale Optoelectronics, Shenzhen University, Shen Zhen, 518060, China

[2]International Iberian Nanotechnology Laboratory (INL), Avenida Mestre José Veiga, Braga, 4715-330, Portugal

[3]Helmholtz-Zentrum Dresden-Rossendorf (HZDR), Institute of Ion Beam Physics and Materials Research, Bautzner Landstrasse 400, D-01328 Dresden, 01328, Germany

[4]Department of Applied Physics, China Agricultural University, Beijing 100080, China

ABSTRACT: Intrinsic two-dimensional (2D) ferromagnets with room temperature ferromagnetism and air stability are highly desirable for spintronic applications. Unfortunately, the experimentally observed intrinsic 2D ferromagnetic materials are very less, and there are fewer materials that have both room temperature ferromagnetism and air stability. Here, intrinsic room-temperature ferromagnetic γ-Fe_2O_3 nanoflakes with different shapes have been successfully grown by the chemical vapor deposition method. Firstly, triangular γ-Fe_2O_3 flakes epitaxially grow on the α-Al_2O_3 surface at low temperature, and the flakes grow gradually in

size and finally form a large-scale γ-Fe_2O_3 film as increasing the growth time. This growth process belongs to thermodynamic control. However, the triangular γ-Fe_2O_3 flakes sequentially transform into stellated, petaloid, and dendritic crystalloids when enhancing the temperature of precursor powder. This transition reveals the growth process from thermodynamically to kinetically dominated control and successfully realizes the morphology tunable synthesis recipe. Additionally, these γ-Fe_2O_3 flakes are ferromagnetic in the range of 5 K to 300 K and own out-of-plane easy magnetization axis. Moreover, compared with the triangular and stellated γ-Fe_2O_3 flakes, the petaloid and dendritic γ-Fe_2O_3 flakes show enhanced coercive force. The γ-Fe_2O_3 nanoflakes with diverse shapes synthesized by controlling temperature have similar resistivity. The synthesis of γ-Fe_2O_3 flakes with different shapes and properties paves the way for the preparation and application of next generation electronic and spintronic devices.

Keywords: γ-Fe_2O_3 Nanoflakes; Morphology tunable synthesis; Room-temperature ferromagnetism; Coercive force; Resistivity

Introduction

Ferromagnets (FMs) advance greatly the development of state-of-the-art electronic and spintronic devices.[1-3] The new generation of memory devices triggers ever-increasing requirements on the dimension of FMs. Recent appearance of two-dimensional (2D) layered materials provides the feasibility of small size and high integration for novel memory devices.[4, 5] The advantage of these 2D layered materials rests with their in-plane atoms linked by strong chemical bonds and their out-of-plane layers linked by a weak van der Waals (vdWs) force.[6, 7] Such an extremely low dimension not only induces unprecedentedly abundant physics but also

reveals a magnificent innovation in ever-smaller electronic and spintronic devices.[8, 9] However, such an intriguing 2D magnetism remains an elusive dream in practice, and these stable 2D crystals are not triggered in real yield yet.[10]

Diverse 2D layered magnetic materials have currently been reported experimentally, e.g. CrI_3,[11-16] Fe_3GeTe_2,[1, 17-19] and $Cr_2Ge_2Te_6$,[20], and accordingly, these 2D magnetic materials have been widely used in electronic and spintronic devices due to their exotic property. Nevertheless, the most studied 2D layered FMs so far are unstable in atmosphere, and their Curie temperature (T_C) is far below room temperature.[21] Recently, a few 2D non-layered materials were achieved using the chemical vapor deposition (CVD), which supposedly solved the issue of air stability. For instance, Cr_2S_3 is an air-stable ferrimagnetic semiconductor.[22-24] In particular, CrSe[25] and Cr_2Te_3[26] behave close to room-temperature T_C (~280 K) in experiments. These experimental studies are of particular interest in that direct synthesis of room-temperature FMs throught the CVD method is key for promoting device utility.[27] Despite that many kinds of 2D layered and non-layered FM-based devices have been demonstrated at low or high temperatures, they are not yet adequately warm to room temperature for electronic and spintronic device applications. A 2D FMs possessing simultaneously ultrathin nature, air stablility, and high T_C is thus timely and ultimately important for a new generation of electronic and spintronic devices.

As an iron oxide, 2D non-layered ε-Fe_2O_3 represents such a kind of FM materials in view of its ultrathin nature and room-temperature Tc.[28] Iron oxide is a species of common material rich in natural resources and nontoxicity,[29] which involves various phases, such as α, β, γ, and ε.[30] Among these phases, γ-Fe_2O_3 is the second most common Fe_2O_3 polymorph in nature that could be applied in tumor treatment,[31] lithium-ion battery,[32] recoverable catalyst,[33] gas sensor,[34]

and magnetic study.[35, 36] It has a cubic crystal structure of an inverse spinel-type and crystallizes in the $P4_132$ space group with a = 8.351 Å and consists of one-third of the tetrahedral sites and two-thirds of the octahedral sits bearing Fe^{3+} cation. Importantly, γ-Fe_2O_3 has a spinel structure with two magnetic sublattices and exhibits ferromagnetism,[30, 37] making it a preferred oxide to fulfill air stability and room-temperature ferromagnetism for ultrathin electronic and spintronic device applications. However, the synthesis of ultrathin room-temperature ferromagnetic γ-Fe_2O_3 materials is scarcely reported due to the difficulty in controlling the growth process and the easy mutual conversion between γ-Fe_2O_3 and α-Fe_2O_3 or oxyhydroxide.[29, 38]

Here, we report the successful synthesis of ultrathin γ-Fe_2O_3 nanoflakes using a facile and efficient growth strategy based upon the CVD method,[2, 39] and demonstrate that ultrathin γ-Fe_2O_3 nanoflakes exhibit diverse morphology as the growth temperature is tuned. Importantly, all these nanoflakes with different shapes show room temperature ferromagnetism. At low temperature, triangular γ-Fe_2O_3 flakes appear and the flakes grow gradually in size and finally form a large-scale γ-Fe_2O_3 film as increasing the growth time. This growth process belongs to thermodynamic control. The triangular γ-Fe_2O_3 flakes sequentially transform into stellated, petaloid, and dendritic crystalloids as increasing the temperature of precursor powder. This transition reveals the growth process from thermodynamically to kinetically dominated control. Moreover, compared with the triangular and stellated γ-Fe_2O_3 flakes, the petaloid and dendritic γ-Fe_2O_3 flakes show enhanced coercive force. The γ-Fe_2O_3 nanoflakes with diverse shapes synthesized by controlling temperature have similar resistivity. The intriguing finding of ultrathin, air-stable, and multifunctional room-temperature 2D non-layered γ-Fe_2O_3 FM and its growth recipe opens up a novel avenue in the practical application of next-generation electronic,

spintronic, and memory devices.

Results and Discussion

γ-Fe_2O_3 can be obtained directly from the oxidation of iron, which can be achieved using a simple CVD system (Figure S1a). Iron and cobalt mixed powder was loaded in a corundum boat, which was placed in the center of the furnace temperature zone. Cobalt can be used as a fluxing medium or catalyst in the synthesis process. The substrate [SiO_2/Si, mica, or sapphire (α-Al_2O_3)] was placed face down on the corundum boat; sapphire was more suitable for γ-Fe_2O_3 nanoflake growth (Figures S1b−d). The nanoflakes were then characterized by optical microscopy (OM), scanning electron microscopy (SEM), Raman spectroscopy, and X-ray photoelectron spectroscopy (XPS). As shown in Figure 1a, the triangular γ-Fe_2O_3 nanoflakes grown on sapphire exhibited a uniform orientation, which might be related to the substrate. To verify this point of view, statistics was performed. Figure S2a shows the photograph of a 2-inch α-Al_2O_3 substrate with a unique polished surface [c-plane (0001)] and a cutting reference edge [α-Al_2O_3 $(11\bar{2}0)$]. The SEM images of the triangular γ-Fe_2O_3 nanoflakes (upper) and the cutting reference edge (lower) are illustrated in Figure S2a, and the green and black arrows represent the crystal edge (zigzag direction) of a γ-Fe_2O_3 nanoflake and the cutting reference edge [α-Al_2O_3 $(11\bar{2}0)$], respectively. θ is the angle between the crystal edge of γ-Fe_2O_3 nanoflakes and the cutting reference edge. The atomic models of γ-Fe_2O_3 and α-Al_2O_3 simulated this growth stacking mode (Figure S2b). The orientations of γ-Fe_2O_3 nanoflakes were strongly coupled with single-crystal facets (Figure S2c), indicating that the γ-Fe_2O_3 nanoflakes epitaxially grew on the α-Al_2O_3 surface, which was attributed to their similar lattice parameters

and lowest formation energy for γ-Fe_2O_3 nanoflakes at $\theta \approx 0$. Our paper demonstrates that the epitaxial growth recipe could promote uniform orientations of γ-Fe_2O_3 grown on single-crystal sapphire. This work is similar to some works that have determined mono-orientated 2D materials by using low-crystalline substrate facets.[40, 41] The triangular nanoflakes were then transferred on a copper grid (Figure 1b) to investigate the structure of γ-Fe_2O_3. As revealed in the high-resolution transmission electron microscopy (HRTEM) image (Figure 1c) collected at the square location in Figure 1b, atoms were distributed in accordance with the honeycomb lattice, and the $(0\bar{2}2)$ interplanar spacing was ~0.3 nm, in fair agreement with the top view of the γ-Fe_2O_3 structure along [111] axis. Given that transmission electron microscopy (TEM) and HRTEM images were collected in the same direction, the edge of the triangular γ-Fe_2O_3 nanoflakes corresponded to the zigzag direction of the crystal, as marked by the white arrows in Figures 1b and c. Figure 1d shows the corresponding fast Fourier transform (FFT) pattern of the HRTEM image, which displays one set of sixfold symmetry diffraction spots. These results agree with those of previous works,[42-44] proving that the triangular nanoflakes are definitely γ-Fe_2O_3 crystals. The Raman spectrum (Figure 1e) of the as-grown triangular nanoflakes exhibits three peaks at ~356, 512, and 650−720 cm^{-1}, except for the contribution from the substrate, they were recognized to arise from T_{2g}, E_g, and A_{1g}, respectively. Two broad peaks appeared at high wavenumbers (~1200 and 1400 cm^{-1}), which might be contributed by the magnon mode.[38, 45, 46] These characteristic peaks are highly consistent with reports on γ-Fe_2O_3 crystals.[47-52] XPS measurements were also performed to explore the chemical state of Fe and O elements. The high-resolution region of Fe 2p (Figure 1f) can be divided into two main peaks at binding energies of 710.71 ($Fe\ 2p_{3/2}$) and 724.25 eV ($Fe\ 2p_{1/2}$) together with two shake-

up satellites at 717.96 and 731.85 eV, which are consistent with the typical values for Fe (III).[53-55] All the peaks were fitted using the Gauss–Lorentz (ratio: 40%) combination formula. The deconvolution spectrum of O 1s (Figure 1g) shows a peak at 531.07 eV, which can be fitted using the Gauss–Lorentz (ratio: 30%) combination formula. The OM, SEM, Raman, and XPS results strongly proved the synthesis of triangular γ-Fe_2O_3 nanoflakes.

A series of morphology images for samples in different growth stages was collected to explore the synthesis process of triangular γ-Fe_2O_3 nanoflakes. Figures 2a–g show the SEM images of γ-Fe_2O_3 nanoflakes synthesized with different growth times. In the initial stage, the γ-Fe_2O_3 nanoflakes showed three related dendrites along specific diffusion pathways (Figure 2a). We inferred that these dendrites were related to the initial clusters. Then, the crystal grew along the edges of the three dendrites. After 5 min of growth, the edges of the crystal displayed a sawtooth shape (Figure 2b). Subsequently, the γ-Fe_2O_3 nanoflakes further grew into a nearly complete triangular shape (Figures 2c and d). As shown in Figures 2e–g, the triangular γ-Fe_2O_3 nanoflakes rapidly grew up and gradually spliced together, eventually forming a large-scale film, this growth process belongs to thermodynamic control.[56, 57] The AFM contour images confirmed this phenomenon. Figure S3a shows the AFM image of the γ-Fe_2O_3 nanoflakes at the initial stage; three branches were growing in three directions, which were formed with tiny triangular sheets. As shown in Figure S3b, the γ-Fe_2O_3 nanoflake obtained through a longer growth time had a triangular shape with three jagged edges. The surface of the γ-Fe_2O_3 nanoflake was uneven, indicating that it was in an immature growth stage. Figure S3c depicts the AFM image of a triangular nanoflake with three sharp edges, in which the traces of three growth pathways (as mentioned in the initial stage) were still faintly visible on its surface. The

thickness of the nanoflakes did not change dramatically during the growth process. Figure 2h shows the relationship plot between nanoflake size and growth time; each data point displayed with a standard error of the mean was counted from multiple nanoflakes. Comparison of the slopes of the two pieces of data (marked with red and blue arrows) indicated that the crystal size increased slowly in the early stage. However, the growth rate was considerably accelerated when the growth time exceeded 11 min. On the basis of the above results, the schematic of the growth recipe of triangular γ-Fe_2O_3 nanoflakes is illustrated in Figure 2i. Many dangling bonds were exposed on the edge of the dendrites at the initial growth stage. Subsequently, iron and oxygen atoms were preferentially navigating to a stable state or an energetically more favorable location along the edges or corners of the dendrites.[58] The fluxing medium (Co) may play an active role in crystal growth.[59] Accordingly, the crystal growth laterally from the dendrite edge would be promoted, facilitating the synthesis of regularly shaped γ-Fe_2O_3 nanoflakes. As the growth time extended, the nanoflakes grew gradually in dimension and merged, forming a large-scale γ-Fe_2O_3 film. These findings are similar to previous reports on other 2D materials.[58, 60-64]

Synthesis of 2D materials by using the CVD method involves many inconstant growth parameters, such as substrate, transport gas, growth time, and cooling rate. In this work, suitable substrate and transport gas (Ar) were selected, and the influence of growth time on triangular nanoflakes was clarified. Furthermore, the precursor temperature acts as a dominant factor for the nanoflake shape and size in the crystallization and growth stage.[65] Figure 3 shows the OM and SEM images of the γ-Fe_2O_3 nanoflakes grown at different temperatures. The overall results indicated that the growth of γ-Fe_2O_3 nanoflakes followed several novel growth

models. Figures 3a–d show some OM images of the four nanoflake models in the initial stage (growth time: ~4 min). The growth temperatures were 930 °C, 980 °C, 1030 °C, and 1080 °C. With prolonged growth time (~15 min), γ-Fe_2O_3 nanoflakes could grow into mature shapes: triangular, stellated, petaloid, and dendritic shapes (Figures 3e–h). As described in the previous section, the triangular γ-Fe_2O_3 domains diverged out along the three diffusion pathways. Nonetheless, the γ-Fe_2O_3 domains tended to grow two sets of related dendrites (six diffusion pathways) derived from the same nucleated cluster when the temperature was set to 980 °C. Finally, the domains grew into stellated crystals, including two triangular crystals with a specific angle of 180°, which were synthesized on the basis of the same nucleated cluster. The γ-Fe_2O_3 domains changed into a petaloid shape when the temperature was increased to 1030 °C. Figures 3c and g present this novel diffusion-limited growth model. The number of dendrites derived from the same nucleated cluster increased significantly, and the nanoflakes grew into petaloid ones along more than sixfold diffusion pathways (displaying a radial pattern). Figures 3d and h represent an exceptional growth model, which was dominated by dendrite growth when the temperature was increased to 1080 °C. In the initial stage (Figure 3d), the γ-Fe_2O_3 nanoflakes grew into a fan-shaped blade. As the growth time increased, the crystal grew chaotically along the dendrites (Figure 3h). The high-magnification OM (Figures 3i–l) and SEM (Figures 3m–p) images of these nanoflakes reveal the shape and size of these triangular, stellated, petaloid, and dendritic nanoflakes. In this work, we have achieved controlled growth of nanoflakes in various shapes, and the temperature is a pivotal factor for tunable morphology.[65] The growth details will be analyzed in the following paragraphs.

To explore the growth path of these shaped γ-Fe_2O_3 nanoflakes, their surface AFM contour

images were collected. Figures 4a–d show the AFM images of triangular, stellated, petaloid, and dendritic nanoflakes with ultrathin thicknesses of ~4.61, 4.15, 8.67, and 5.31 nm, respectively. The high-magnification AFM images (Figures 4e–h) display the surface details of the nanoflakes with four morphologies. The yellow arrows delineate the growth direction of γ-Fe_2O_3 nanoflakes. Figure 4e confirms that the triangular γ-Fe_2O_3 nanoflake grew along three diffusion pathways. The AFM images (Figures 4b and f) show the surface of the stellated nanoflake similar to two triangular Lego blocks rotationally aligned and stacked together. The yellow arrow marked in Figure 4f reveals a similar growth model compared with the triangular nanoflake. In accordance with the introduction in the previous chapter, the triangular γ-Fe_2O_3 nanoflake had an epitaxial relationship with the sapphire substrate. Hence, the stellated nanoflake can be understood as two triangular γ-Fe_2O_3 nanoflakes grown on a substrate similar to AA- and AB-stacking configurations. The petaloid γ-Fe_2O_3 nanoflake (Figure 4c) looked like a fresh blooming flower; its petals stretched out from the central cluster along the diffusion pathway (the yellow arrow marked in Figure 4g). Some upstretched "boundaries" existed among the petals. Figures S4a and b show the SEM images of two multipetaloid γ-Fe_2O_3 nanoflakes, which were grown following a typical diffusion-limited model. Similar petaloid graphene has also been reported, and this appearance is mostly caused by mutations in growth conditions.[58, 63, 66] The chaotic growth state on the surface of dendritic γ-Fe_2O_3 nanoflakes (Figures 4d and f) indicated that the morphology of this nanoflake was difficult to control, although they exhibited sharp fan-shaped dendrites in the initial stage (Figures S4c and d). However, the dendritic γ-Fe_2O_3 nanoflake whose morphology is difficult to control is not the focus of this work.

On the basis of the descriptions of morphological characteristics and growth processes, we depicted a schematic (Figure 4i) for the four growth models. Such unique morphological characteristics were intuitively associated with the furnace temperature, that is, with the temperature of iron powder, the vapor pressure of iron in the tube was directly related to the temperature positively. The increase in temperature for the iron powder could cause the enlargement of nucleated clusters (Figures 4b and c) and the improvement of the growth rate of crystals. This viewpoint can be testified in the energy-dispersive spectroscopy maps shown in Figure S5. The iron content in the core of stellated and petaloid γ-Fe_2O_3 nanoflakes obtained at high temperature was considerably high. The size of the nanoflakes grown under high-temperature conditions was larger than others with the same growth time. The triangular γ-Fe_2O_3 flakes sequentially transform into stellated, petaloid, and dendritic crystalloids when enhancing the temperature of precursor powder and breaking the balance of the growth conditions (Figure 4i). This transition reveals the growth process from thermodynamically to kinetically dominated control and successfully realizes the morphology tunable synthesis recipe.[56, 67]

The γ-Fe_2O_3 nanoflakes are air-stable materials that can be stored stably in the air for approximately 3 months (Figure S6).

Raman spectra and mapping images were collected to study the composition of the four shaped nanoflakes. Five uniform characteristic peaks exist in the Raman spectra of triangular, stellated, petaloid, and dendritic nanoflakes (Figure S7), proving the synthesis of γ-Fe_2O_3. Figure 5 provides the mapping images of Raman peak intensity, position, and width for triangular, stellated, and petaloid γ-Fe_2O_3 nanoflakes. The intensity, position, and width

mapping images (Figures 5a–c) of Raman A_{1g} peak for triangular γ-Fe_2O_3 nanoflakes exhibit a uniform signal distribution. As revealed in Figures 5d and g, the intensity signal of Raman A_{1g} peak for the centers of stellated and petaloid γ-Fe_2O_3 nanoflakes was considerably enhanced, which might be attributed to the existence of nucleated clusters. A uniform distribution of Raman A_{1g} peak in position and width signal was also observed (Figures 5e, f, h, and i). Figure 5g presents that the Raman signal at the "boundaries" of the petaloid γ-Fe_2O_3 nanoflake showed an unusual weak enhancement; thus, we collected some Raman spectra at these positions (spectra I–III in Figure S8). These Raman spectra could be deconvoluted to 14 Lorentz peaks; 3 of them (at ~419, 579, and 754 cm^{-1}) were contributed by sapphire. The extracted peak position, normalized intensity, and width of the 11 other peaks in Figure S8b are highly consistent with those of previously reported Raman curves for α-Fe_2O_3.[51, 68-70] A broad peak exists at ~650–720 cm^{-1} in the Raman spectra of α-Fe_2O_3 and γ-Fe_2O_3; consequently, the two phases with the mapping images of the peak at this position are difficult to distinguish. For this reason, the typical Raman peak (~1315 cm^{-1}) of α-Fe_2O_3 was selected to plot the intensity, position, and width mapping images (Figures 5j–l), which proved that α-Fe_2O_3 appeared at the "boundaries" and core of the petaloid nanoflake. Raman spectra IV and V in Figure S8 were collected at the edge of dendritic nanoflakes. These observations indicated that the triangular, stellated, petaloid, and dendritic nanoflakes were all γ-Fe_2O_3, but the petaloid and dendritic nanoflakes contained a small amount of α-Fe_2O_3.

To gain a deep insight into the oxidation state of iron, we conducted XPS measurements on the as-grown triangular, stellated, petaloid, and dendritic nanoflakes (Figure S9). Figures S9a and b are the high-resolution XPS spectra of Fe and O elements for triangular nanoflakes,

which have been introduced in the previous chapter. Figures S9c, e, and g show the chemical state of Fe element for stellated, petaloid, and dendritic nanoflakes, respectively. All the peaks were fitted using the Gauss–Lorentz (ratio: 40%) combination formula. The corresponding high-resolution XPS spectra of the O1s region (Figures S9d, f, and h) have only one peak, which was fitted using the Gauss–Lorentz (ratio: 30%) combination formula. Table S1 lists all the fitting results of the chemical state for Fe 2p and O 1s. The longitudinal comparison indicated that the position and full width at half maximum of each peak were homogeneous, indicating the purity of synthetic γ-Fe_2O_3 nanoflakes.

γ-Fe_2O_3 is a traditional intrinsic FM.[35, 71-73] We performed magnetic hysteresis (*M*-*H*) loop measurements to verify the magnetic performance of the straticulate γ-Fe_2O_3 nanoflakes. Figures S10–13 show the normal state *M*-*H* loops of triangular, stellated, petaloid, and dendritic γ-Fe_2O_3 nanoflakes, indicating that these γ-Fe_2O_3 nanoflakes were ferromagnetic in the range of 5 K to 300 K. The diamagnetic contribution from the Al_2O_3 substrate was subtracted. To deepen the magnetic understanding of γ-Fe_2O_3 nanoflakes, the H_C, saturation magnetization (M_S), and remnant magnetization (M_R) in vertical ($\perp$, out-of-plane) and parallel (//, in-plane) magnetic fields were also extracted and plotted. Figures 6a and b show the *M*-*H* loops at 5 K in vertical and parallel magnetic fields, respectively; Figures 6c and d are the *M*-*H* loops at 300 K in vertical and parallel magnetic fields, respectively. These figures demonstrate that the magnetic moment and saturation magnetization (M_S) of the triangular, stellated, petaloid, and dendritic γ-Fe_2O_3 nanoflakes increased in turn. The parallel magnetic field led to steep slopes for *M*-*H* loops in the near-zero magnetic field. The difficulty of magnetizing an FM in the direction of a crystal axis can be represented by the energy required to magnetize a unit FM to

saturation (E_M). The larger E_M is, the more difficult it is to magnetize, and vice versa. E_M can be expressed as follows:

$$E_M = \frac{W}{V} = \frac{1}{V}\int_0^{M_S} H\, dM,$$

where W is the work done in the magnetization process, which is also the area between the initial M-H curve and the M axis; V means the volume of the FM; M_S represents the saturation magnetization; and H represents the initial M-H curve. As shown in Figure S14, the work required for complete magnetization of petaloid γ-Fe_2O_3 nanoflakes in vertical and parallel magnetic fields at 5 K indicated that minimal work needs to be done in vertical and magnetic fields. Therefore, out-of-plane is the easy magnetization axis for γ-Fe_2O_3 nanoflakes, which is consistent with the fact that the M-H curves exhibit great H_C in vertical and magnetic fields. Figures 6e and f summarize the relationship between H_C and temperature of the triangular, stellated, petaloid, and dendritic γ-Fe_2O_3 nanoflakes in vertical and parallel magnetic fields, respectively. H_C increased with the decrease in temperature. Compared with the triangular and stellated γ-Fe_2O_3 nanoflakes, the petaloid and dendritic γ-Fe_2O_3 nanoflakes showed strong H_C; this condition may be attributed to the existence of a small amount of α-Fe_2O_3 in the petaloid and dendritic γ-Fe_2O_3 nanoflakes, which corresponded to the growth process transition from thermodynamics to kinetics. In particular, α-Fe_2O_3 has exhibited ferromagnetism in some cases.[74-76] This method of adjusting H_C in a large range by changing the shape of γ-Fe_2O_3 nanoflakes is an interesting event for the application of 2D γ-Fe_2O_3 nanoflakes.

We further investigated the magnetoelectric performance of the γ-Fe_2O_3 nanoflakes that were used in this study and synthesized at 930 °C and 980 °C; metal electrodes (Cr/Au) were then fabricated on top by using standard photoetching (Figures 7a and b). The electrical

transport data were from 400 K to low temperature were adopted. Figure 7c is the Hall resistance (R_H) response of a triangular γ-Fe_2O_3 device (Figures 7a and b) to a magnetic field sweep, which exhibited a feeble classical rectangular hysteresis loop at room temperature (300 K). As shown in Figure 7d, the electrical resistivity (ρ) of the triangular γ-Fe_2O_3 device rapidly increased monotonously with decreasing temperature in the whole temperature range, presenting typical semiconductive performance ($\rho = R_{xx}S/L$, where R_{xx} is the longitudinal resistance, S is the cross-sectional area, and L represents the length of the device).[26] These ρ-T curves are relatively close even if the device (Figure S15) thickness is different. Figure 7e exhibits that the ρ depended on the thickness of triangular and petaloid γ-Fe_2O_3 devices (Figure S16), indicating that the two morphologies of γ-Fe_2O_3 nanoflakes show consistent resistivity. In general, the triangular γ-Fe_2O_3 nanoflakes exhibit room-temperature intrinsic ferromagnetism and semiconductive performance, and their resistance can be effectively adjusted by changing the temperature. The γ-Fe_2O_3 nanoflakes with diverse shapes synthesized by controlling temperature have similar resistivity.

Conclusions

We achieved epitaxial growth of 2D nonlayered triangular γ-Fe_2O_3 nanoflakes on sapphire. Their lateral size is mainly affected by growth time. The γ-Fe_2O_3 nanoflakes can be controlled by increasing the precursor temperature to exhibit triangular, stellated, petaloid, and dendritic shapes in sequence, which represent a morphology tunable transition process from thermodynamically to kinetically dominated control. Although all the γ-Fe_2O_3 nanoflakes exhibit room-temperature ferromagnetism, the petaloid and dendritic γ-Fe_2O_3 nanoflakes show

strong H_C compared with the triangular and stellated γ-Fe_2O_3 nanoflakes. This difference may be attributed to the existence of a small amount of α-Fe_2O_3 in the petaloid and dendritic γ-Fe_2O_3 nanoflakes. The triangular γ-Fe_2O_3 nanoflakes exhibit room-temperature intrinsic ferromagnetism and semiconductive performance, and their resistance can be effectively adjusted by changing the temperature. Various γ-Fe_2O_3 nanoflakes synthesized at different temperatures show room-temperature intrinsic ferromagnetism and have similar electrical resistivity. Our work provides a fundamental understanding of control synthesis and performance for 2D nonlayered γ-Fe_2O_3 nanoflakes. Overall, the synthesis of ultrathin, air-stable, and room-temperature ferromagnetic γ-Fe_2O_3 nanoflakes with different shapes and properties paves the way for the preparation and application of next generation electronic and spintronic devices.

METHODS

Growth of γ-Fe_2O_3 nanoflakes and Films. The γ-Fe_2O_3 nanoflakes were grown on α-Al_2O_3 substrates in a home-made chemical vapor deposition (CVD) system (Figure S1a). A corundum boat containing mixed powder of 0.035 g Fe (99.9%, Alfa Aesar) and 0.01 g Co (99.8%, Alfa Aesar) was placed in the temperature zone, and the cleaned α-Al_2O_3 (*c*-plane (0001)) substrate was face-down covered on the corundum boat. Before heating, the CVD system was evacuated and then flushed with 200 sccm of high-purity argon gas for 30 min to remove air and other impurities. After purging the system, the furnace was heated to 930~1080°C. In the meanwhile, 50 sccm argon gas was introduced in the CVD system as carrier gas under atmospheric pressure. The reaction time ranged from 3 to 30 min, and the high-temperature system was cooled down

naturally to room temperature. The γ-Fe_2O_3 nanoflakes or films were eventually obtained.

Structural characterization. OM images were taken using an optical microscope (PSM-1000, Moti) equipped with three long focal length lenses (×10, ×50, and ×100). Raman spectra were obtained using a confocal Raman microscope (Alpha 300R, WITec) with a 532 nm laser, and the laser power was measured by using a hand-held optical power meter console (PM100D, Thorlabs). The laser spot diameter was 1 μm. XRD analyses were performed using an X-Ray Diffractometer (X PERT PRO MRD S4, PANalytical). XPS measurements were conducted on a spectrometer (ESCALAB 250Xi, Thermo Scientific) with Al K_α X-rays (1489.6 eV). SEM images were taken using a field-emission scanning electron microscope (QUANTA 650FEG, FEI). AFM images were obtained using an atomic force microscope (Icon, Bruker). TEM and HRTEM observations were carried out by a transmission electron microscope (JEM-2100, JEOL). The TEM specimen was prepared by the standard wet transfer method.

Device Fabrication and property measurement. The Hall patterns were fabricated using the standard photolithography with the help of direct-write laser-based micro-fabrication system (DWL 2000, Heidelberg Instruments) and Photoresist Coater (Gamma Cluster System, Karls SUSS MicroTec). The Cr/Au (10/70 nm) metal electrodes were then sputtered on top using a multitarget confocal magnetron sputter (UHV PVD, Kenosistec). Magnetization measurements were performed by using a commercial superconducting quantum interference device (SQUID) (MOMS 3, QUANTUM DESIGN) with the magnetic field either vertical (out-of-plane) or parallel (in-plane) to the nanoflakes. The Al_2O_3 substrates covered by γ-Fe_2O_3 nanoflakes were diced to 3 × 5 mm^2 chips and loaded into a hollow copper rod. The magnetic hysteresis loops were measured from 5 K to 300 K while cycling a DC magnetic field through -2 T to 2 T. The

magnetoelectric data were collected by using a Hall measurement system (HMS 9709A, Lake Shore), where magnetic field was applied parallel to the nanoflakes in measurement.

Author Contributions

Z.C.W., W.J.W., and Y.L. initiated and managed the project. Z.Y.J., W.J.W., and Z.C.W. completed the sample growth, characterization, device fabrication and prepared the manuscript. Z.C.L. and W.J.W. performed the magnetic and magnetoelectric measurements. All authors discussed the results and directed the entire study.

ORCID IDs and E-mails

Zhiyan Jia: 0000-0002-8201-7644, jiazhiyan8@szu.edu.cn

Zichao Li: zichao.li@hzdr.de

Rong Sun: rong.sun@inl.int

Chenliang Su: 0000-0002-8453-1938, chmsuc@szu.edu.cn

Shengqiang Zhou: 0000-0002-4885-799X, s.zhou@hzdr.de

Francis Leonard Deepak: Leonard.Francis@inl.int

Ying Li: queenly@szu.edu.cn

Wenjie Wang: wenjie.wang@cau.edu.cn

Zhongchang Wang: 0000-0003-2141-4803, zhongchang.wang@inl.int

Notes

The authors declare no competing financial interest.

*To whom correspondence should be addressed. E-mails: zhongchang.wang@inl.int (Z.C.W.);

queenly@szu.edu.cn (Y.L.); wenjie.wang@cau.edu.cn (W.J.W.)

Acknowledgments

We appreciate the financial supports from the Projects funded by the National Natural Science Foundation of China (NSFC) (51728202, 51732010, 51672240, and 51801175). Z.C.W. and F.L.D. acknowledge the project Nanotechnology-Based Functional Solutions (NORTE-01-0145-FEDER-000019), supported by Norte Portugal Regional Operational Programme (NORTE2020) under the PORTUGAL 2020 Partnership Agreement through the European Regional Development Fund (ERDF). Z.Y.J. thanks financial subsidy by China Postdoctoral Science Foundations (2019TQ0207 and 2019M663057) and is supported by the International Postdoctoral Exchange Fellowship Program (2020062) from the China Postdoctoral Council.

References

(1) Deng, Y.; Yu, Y.; Song, Y.; Zhang, J.; Wang, N. Z.; Sun, Z.; Yi, Y.; Wu, Y. Z.; Wu, S.; Zhu, J.; Wang, J.; Chen, X. H.; Zhang, Y. Gate-tunable room-temperature ferromagnetism in two-dimensional Fe_3GeTe_2. *Nature* **2018**, *563*, 94-99.

(2) Fu, S.; Kang, K.; Shayan, K.; Yoshimura, A.; Dadras, S.; Wang, X.; Zhang, L.; Chen, S.; Liu, N.; Jindal, A.; Li, X.; Pasupathy, A. N.; Vamivakas, A. N.; Meunier, V.; Strauf, S.; Yang, E.-H. Enabling room temperature ferromagnetism in monolayer MoS_2 via in situ iron-doping. *Nat. Commun.* **2020**, *11*, 2034.

(3) Ostwal, V.; Shen, T.; Appenzeller, J. Efficient spin-orbit torque switching of the semiconducting van der Waals ferromagnet $Cr_2Ge_2Te_6$. *Adv. Mater.* **2020**, *32*, 1906021.

(4) Novoselov, K. S.; Geim, A. K.; Morozov, S. V.; Jiang, D.; Zhang, Y.; Dubonos, S. V.; Grigorieva, I. V.; Firsov, A. A. Electric field effect in atomically thin carbon films. *Science* **2004**, *306*, 666-669.

(5) Li, C.; Chen, C.; Chen, J.; He, T.; Li, H.; Yang, Z.; Xie, L.; Wang, Z.; Zhang, K. High-performance junction field-effect transistor based on black phosphorus/β-Ga_2O_3 heterostructure. *J. Semicond.* **2020**, *41*, 082002.

(6) Novoselov, K. S.; Mishchenko, A.; Carvalho, A.; Castro Neto, A. H. 2D materials and van der Waals heterostructures. *Science* **2016**, *353*, aac9439.

(7) Tan, C.; Cao, X.; Wu, X.-J.; He, Q.; Yang, J.; Zhang, X.; Chen, J.; Zhao, W.; Han, S.; Nam, G.-H.; Sindoro, M.; Zhang, H. Recent advances in ultrathin two-dimensional nanomaterials.

Chem. Rev. **2017**, *117*, 6225-6331.
(8) Feng, Y. P.; Shen, L.; Yang, M.; Wang, A.; Zeng, M.; Wu, Q.; Chintalapati, S.; Chang, C.-R. Prospects of spintronics based on 2D materials. *WIREs Comput. Mol. Sci.* **2017**, *7*, e1313.
(9) Zhou, Z.; Cui, Y.; Tan, P.-H.; Liu, X.; Wei, Z. Optical and electrical properties of two-dimensional anisotropic materials. *J. Semicond.* **2019**, *40*, 061001.
(10) Gibertini, M.; Koperski, M.; Morpurgo, A. F.; Novoselov, K. S. Magnetic 2D materials and heterostructures. *Nat. Nanotechnol.* **2019**, *14*, 408-419.
(11) Huang, B.; Clark, G.; Navarro-Moratalla, E.; Klein, D. R.; Cheng, R.; Seyler, K. L.; Zhong, D.; Schmidgall, E.; McGuire, M. A.; Cobden, D. H.; Yao, W.; Xiao, D.; Jarillo-Herrero, P.; Xu, X. Layer-dependent ferromagnetism in a van der Waals crystal down to the monolayer limit. *Nature* **2017**, *546*, 270-273.
(12) Seyler, K. L.; Zhong, D.; Klein, D. R.; Gao, S.; Zhang, X.; Huang, B.; Navarro-Moratalla, E.; Yang, L.; Cobden, D. H.; McGuire, M. A.; Yao, W.; Xiao, D.; Jarillo-Herrero, P.; Xu, X. Ligand-field helical luminescence in a 2D ferromagnetic insulator. *Nat. Phys.* **2017**, *14*, 277-281.
(13) Huang, B.; Clark, G.; Klein, D. R.; MacNeill, D.; Navarro-Moratalla, E.; Seyler, K. L.; Wilson, N.; McGuire, M. A.; Cobden, D. H.; Xiao, D.; Yao, W.; Jarillo-Herrero, P.; Xu, X. Electrical control of 2D magnetism in bilayer CrI_3. *Nat. Nanotechnol.* **2018**, *13*, 544-548.
(14) Jiang, S.; Shan, J.; Mak, K. F. Electric-field switching of two-dimensional van der Waals magnets. *Nat. Mater.* **2018**, *17*, 406-410.
(15) Kim, H. H.; Yang, B.; Patel, T.; Sfigakis, F.; Li, C.; Tian, S.; Lei, H.; Tsen, A. W. One million percent tunnel magnetoresistance in a magnetic van der Waals heterostructure. *Nano Lett.* **2018**, *18*, 4885-4890.
(16) Wang, Z.; Gutierrez-Lezama, I.; Ubrig, N.; Kroner, M.; Gibertini, M.; Taniguchi, T.; Watanabe, K.; Imamoglu, A.; Giannini, E.; Morpurgo, A. F. Very large tunneling magnetoresistance in layered magnetic semiconductor CrI_3. *Nat. Commun.* **2018**, *9*, 2516.
(17) Fei, Z.; Huang, B.; Malinowski, P.; Wang, W.; Song, T.; Sanchez, J.; Yao, W.; Xiao, D.; Zhu, X.; May, A. F.; Wu, W.; Cobden, D. H.; Chu, J. H.; Xu, X. Two-dimensional itinerant ferromagnetism in atomically thin Fe_3GeTe_2. *Nat. Mater.* **2018**, *17*, 778-782.
(18) Wang, Z.; Sapkota, D.; Taniguchi, T.; Watanabe, K.; Mandrus, D.; Morpurgo, A. F. Tunneling spin valves based on Fe_3GeTe_2/hBN/Fe_3GeTe_2 van der Waals heterostructures. *Nano lett.* **2018**, *18*, 4303-4308.
(19) Wang, Z.; Zhang, T.; Ding, M.; Dong, B.; Li, Y.; Chen, M.; Li, X.; Huang, J.; Wang, H.; Zhao, X.; Li, Y.; Li, D.; Jia, C.; Sun, L.; Guo, H.; Ye, Y.; Sun, D.; Chen, Y.; Yang, T.; Zhang, J.; Ono, S.; Han, Z.; Zhang, Z. Electric-field control of magnetism in a few-layered van der Waals ferromagnetic semiconductor. *Nat. Nanotechnol.* **2018**, *13*, 554-559.
(20) Gong, C.; Kim, E. M.; Wang, Y.; Lee, G.; Zhang, X. Multiferroicity in atomic van der Waals heterostructures. *Nat. Commun.* **2019**, *10*, 2657.
(21) Li, H.; Ruan, S.; Zeng, Y. J. Intrinsic van der Waals magnetic materials from bulk to the 2D limit: new frontiers of spintronics. *Adv. Mater.* **2019**, *31*, 1900065.
(22) Chu, J.; Zhang, Y.; Wen, Y.; Qiao, R.; Wu, C.; He, P.; Yin, L.; Cheng, R.; Wang, F.; Wang, Z.; Xiong, J.; Li, Y.; He, J. Sub-millimeter-Scale Growth of One-Unit-Cell-Thick Ferrimagnetic Cr_2S_3 Nanosheets. *Nano Lett.* **2019**, *19*, 2154-2161.
(23) Cui, F.; Zhao, X.; Xu, J.; Tang, B.; Shang, Q.; Shi, J.; Huan, Y.; Liao, J.; Chen, Q.; Hou,

Y.; Zhang, Q.; Pennycook, S. J.; Zhang, Y. Controlled growth and thickness-dependent conduction-type transition of 2D ferrimagnetic Cr_2S_3 semiconductors. *Adv. Mater.* **2019**, *32*, 1905896.
(24) Zhou, S.; Wang, R.; Han, J.; Wang, D.; Li, H.; Gan, L.; Zhai, T. Ultrathin non-van der Waals magnetic rhombohedral Cr_2S_3: space-confined chemical vapor deposition synthesis and Raman scattering investigation. *Adv. Funct. Mater.* **2019**, *29*, 1805880.
(25) Zhang, Y.; Chu, J.; Yin, L.; Shifa, T. A.; Cheng, Z.; Cheng, R.; Wang, F.; Wen, Y.; Zhan, X.; Wang, Z.; He, J. Ultrathin magnetic 2D single‐crystal CrSe. *Adv. Mater.* **2019**, *31*, 1900056.
(26) Wen, Y.; Liu, Z.; Zhang, Y.; Xia, C.; Zhai, B.; Zhang, X.; Zhai, G.; Shen, C.; He, P.; Cheng, R.; Yin, L.; Yao, Y.; Getaye Sendeku, M.; Wang, Z.; Ye, X.; Liu, C.; Jiang, C.; Shan, C.; Long, Y.; He, J. Tunable room-temperature ferromagnetism in two-dimensional Cr_2Te_3. *Nano Lett.* **2020**, *20*, 3130-3139.
(27) Jiang, H.; Zhang, P.; Wang, X.; Gong, Y. Synthesis of magnetic two-dimensional materials by chemical vapor deposition. *Nano Res.* **2020**.
(28) Yuan, J.; Balk, A.; Guo, H.; Fang, Q.; Patel, S.; Zhao, X.; Terlier, T.; Natelson, D.; Crooker, S.; Lou, J. Room-temperature magnetic order in air-stable ultrathin iron oxide. *Nano Lett.* **2019**, *19*, 3777-3781.
(29) Hu, Q.; Kim, D. Y.; Yang, W.; Yang, L.; Meng, Y.; Zhang, L.; Mao, H. K. FeO_2 and FeOOH under deep lower-mantle conditions and Earth's oxygen-hydrogen cycles. *Nature* **2016**, *534*, 241-244.
(30) Machala, L.; Tuček, J.; Zbořil, R. Correction to Polymorphous Transformations of Nanometric Iron(III) Oxide: A Review. *Chem. Mater.* **2011**, *23*, 4271-4271.
(31) Jang, J.-t.; Lee, J.; Seon, J.; Ju, E.; Kim, M.; Kim, Y. I.; Kim, M. G.; Takemura, Y.; Arbab, A. S.; Kang, K. W.; Park, K. H.; Paek, S. H.; Bae, S. Giant magnetic heat Induction of magnesium-doped γ-Fe_2O_3 superparamagnetic nanoparticles for completely killing tumors. *Adv. Mater.* **2018**, *30*, 1704362.
(32) Wu, D.; Niu, Y.; Wang, C.; Wu, H.; Li, Q.; Chen, Z.; Xu, B.; Li, H.; Zhang, L. Y. γ-Fe_2O_3 nanoparticles stabilized by holey reduced graphene oxide as a composite anode for lithium-ion batteries. *J. Colloid Interface Sci.* **2019**, *552*, 633-638.
(33) Bartolome, L.; Imran, M.; Lee, K. G.; Sangalang, A.; Ahn, J. K.; Kim, D. H. Superparamagnetic γ-Fe_2O_3 nanoparticles as an easily recoverable catalyst for the chemical recycling of PET. *Green Chem.* **2014**, *16*, 279-286.
(34) Li, Q.; Li, Z.; Zhang, Q.; Zheng, L.; Yan, W.; Liang, X.; Gu, L.; Chen, C.; Wang, D.; Peng, Q.; Li, Y. Porous γ-Fe_2O_3 nanoparticle decorated with atomically dispersed platinum: Study on atomic site structural change and gas sensor activity evolution. *Nano Res.* **2020**.
(35) Prado, Y.; Daffe, N.; Michel, A.; Georgelin, T.; Yaacoub, N.; Greneche, J. M.; Choueikani, F.; Otero, E.; Ohresser, P.; Arrio, M. A.; Cartier-dit-Moulin, C.; Sainctavit, P.; Fleury, B.; Dupuis, V.; Lisnard, L.; Fresnais, J. Enhancing the magnetic anisotropy of maghemite nanoparticles via the surface coordination of molecular complexes. *Nat. Commun.* **2015**, *6*, 10139.
(36) Jeong, U.; Teng, X.; Wang, Y.; Yang, H.; Xia, Y. Superparamagnetic colloids: controlled synthesis and niche applications. *Adv. Mater.* **2007**, *19*, 33-60.
(37) Lee, J.; Kwak, S.-Y. Mn-Doped Maghemite (γ-Fe_2O_3) from Metal–Organic Framework

Accompanying Redox Reaction in a Bimetallic System: The Structural Phase Transitions and Catalytic Activity toward NO_x Removal. *ACS Omega* **2018**, *3*, 2634-2640.
(38) El Mendili, Y.; Bardeau, J. F.; Randrianantoandro, N.; Greneche, J. M.; Grasset, F. Structural behavior of laser-irradiated γ-Fe_2O_3 nanocrystals dispersed in porous silica matrix : γ-Fe_2O_3 to α-Fe_2O_3 phase transition and formation of ε-Fe_2O_3. *Sci. Technol. Adv. Mater.* **2016**, *17*, 597-609.
(39) Yun, S. J.; Duong, D. L.; Ha, D. M.; Singh, K.; Phan, T. L.; Choi, W.; Kim, Y.-M.; Lee, Y. H. Ferromagnetic order at room temperature in monolayer WSe_2 semiconductor via vanadium Dopant. *Adv. Sci.* **2020**, *7*, 1903076.
(40) Qin, B.; Ma, H.; Hossain, M.; Zhong, M.; Xia, Q.; Li, B.; Duan, X. Substrates in the synthesis of two-dimensional materials via chemical vapor deposition. *Chem. Mater.* **2020**, *32*, 10321-10347.
(41) Dumcenco, D.; Ovchinnikov, D.; Marinov, K.; Lazić, P.; Gibertini, M.; Marzari, N.; Sanchez, O. L.; Kung, Y.-C.; Krasnozhon, D.; Chen, M.-W.; Bertolazzi, S.; Gillet, P.; Fontcuberta i Morral, A.; Radenovic, A.; Kis, A. Large-area epitaxial monolayer MoS_2. *ACS Nano* **2015**, *9*, 4611-4620.
(42) Cao, D.; Li, H.; Pan, L.; Li, J.; Wang, X.; Jing, P.; Cheng, X.; Wang, W.; Wang, J.; Liu, Q. High saturation magnetization of γ-Fe_2O_3 nano-particles by a facile one-step synthesis approach. *Sci. Rep.* **2016**, *6*, 32360.
(43) Wang, J.; Ma, Y.; Watanabe, K. Magnetic-field-induced synthesis of magnetic γ-Fe_2O_3 nanotubes. *Chem. Mater.* **2008**, *20*, 20-22.
(44) Zhu, W.; Winterstein, J.; Maimon, I.; Yin, Q.; Yuan, L.; Kolmogorov, A. N.; Sharma, R.; Zhou, G. Atomic structural evolution during the reduction of α-Fe_2O_3 nanowires. *J. Phys. Chem. C* **2016**, *120*, 14854-14862.
(45) El Mendili, Y.; Bardeau, J. F.; Randrianantoandro, N.; Gourbil, A.; Greneche, J. M.; Mercier, A. M.; Grasset, F. New evidences of in situ laser irradiation effects on γ-Fe_2O_3 nanoparticles: a Raman spectroscopic study. *J. Raman Spectrosc.* **2011**, *42*, 239-242.
(46) Dunn, D. S.; Bogart, M. B.; Brossia, C. S.; Cragnolino, G. A. Corrosion of Iron under alternating wet and dry conditions. *Corrosion* **2000**, *56*, 470-481.
(47) Sharifi, T.; Gracia-Espino, E.; Barzegar, H. R.; Jia, X.; Nitze, F.; Hu, G.; Nordblad, P.; Tai, C. W.; Wagberg, T. Formation of nitrogen-doped graphene nanoscrolls by adsorption of magnetic γ-Fe_2O_3 nanoparticles. *Nat. Commun.* **2013**, *4*, 2319.
(48) Testa-Anta, M.; Ramos-Docampo, M. A.; Comesaña-Hermo, M.; Rivas-Murias, B.; Salgueiriño, V. Raman spectroscopy to unravel the magnetic properties of iron oxide nanocrystals for bio-related applications. *Nanoscale Adv.* **2019**, *1*, 2086-2103.
(49) Gervits, N. E.; Gippius, A. A.; Tkachev, A. V.; Demikhov, E. I.; Starchikov, S. S.; Lyubutin, I. S.; Vasiliev, A. L.; Chekhonin, V. P.; Abakumov, M. A.; Semkina, A. S.; Mazhuga, A. G. Magnetic properties of biofunctionalized iron oxide nanoparticles as magnetic resonance imaging contrast agents. *Beilstein J. Nanotechnol.* **2019**, *10*, 1964-1972.
(50) Sklute, E. C.; Kashyap, S.; Dyar, M. D.; Holden, J. F.; Tague, T.; Wang, P.; Jaret, S. J. Spectral and morphological characteristics of synthetic nanophase iron (oxyhydr) oxides. *Phys. Chem. Miner.* **2018**, *45*, 1-26.
(51) Kumar, P.; No-Lee, H.; Kumar, R. Synthesis of phase pure iron oxide polymorphs thin films and their enhanced magnetic properties. *J. Mater. Sci. Mater. Electron.* **2014**, *25*, 4553-

4561.
(52) Jubb, A. M.; Allen, H. C. Vibrational spectroscopic characterization of hematite, maghemite, and magnetite thin films produced by vapor deposition. *ACS Appl. Mater. Inter.* **2010**, *2*, 2804-2812.
(53) Hyeon, T.; Lee, S. S.; Park, J.; Chung, Y.; Na, H. B. Synthesis of highly crystalline and monodisperse maghemite nanocrystallites without a size-selection process. *J. Am. Chem. Soc.* **2001**, *123*, 12798-12801.
(54) Han, Q.; Liu; Xu; Chen; Wang; Zhang, H. Growth and properties of single-crystalline γ-Fe_2O_3 nanowires. *J. Phys. Chem. C* **2007**, *111*, 5034-5038.
(55) Sun, G.; Dong, B.; Cao, M.; Wei, B.; Hu, C. Hierarchical dendrite-like magnetic materials of Fe_3O_4, γ-Fe_2O_3, and Fe with high performance of microwave absorption. *Chem. Mater.* **2011**, *23*, 1587-1593.
(56) Xie, S.; Xu, M.; Liang, T.; Huang, G.; Wang, S.; Xue, G.; Meng, N.; Xu, Y.; Chen, H.; Ma, X.; Yang, D. A high-quality round-shaped monolayer MoS_2 domain and its transformation. *Nanoscale* **2016**, *8*, 219-225.
(57) Ji, Q.; Zhang, Y.; Zhang, Y.; Liu, Z. Chemical vapour deposition of group-VIB metal dichalcogenide monolayers: engineered substrates from amorphous to single crystalline. *Chem. Soc. Rev.* **2015**, *44*, 2587-2602.
(58) Wu, B.; Geng, D.; Xu, Z.; Guo, Y.; Huang, L.; Xue, Y.; Chen, J.; Yu, G.; Liu, Y. Self-organized graphene crystal patterns. *NPG Asia Mater.* **2013**, *5*, e36.
(59) Li, S.; Lin, Y. C.; Zhao, W.; Wu, J.; Wang, Z.; Hu, Z.; Shen, Y.; Tang, D. M.; Wang, J.; Zhang, Q.; Zhu, H.; Chu, L.; Zhao, W.; Liu, C.; Sun, Z.; Taniguchi, T.; Osada, M.; Chen, W.; Xu, Q. H.; Wee, A. T. S.; Suenaga, K.; Ding, F.; Eda, G. Vapour-liquid-solid growth of monolayer MoS_2 nanoribbons. *Nat. Mater.* **2018**, *17*, 535-542.
(60) Jia, Z.; Dong, J.; Liu, L.; Xiang, J.; Nie, A.; Wen, F.; Mu, C.; Wang, B.; Zhai, K.; Yu, Z.; Kang, M.; Liu, Z. One-step growth of wafer-scale monolayer tungsten disulfide via hydrogen sulfide assisted chemical vapor deposition. *Appl. Phys. Lett.* **2019**, *115*, 163104.
(61) Zhang, Y.; Ji, Q.; Han, G.-F.; Ju, J.; Shi, J.; Ma, D.; Sun, J.; Zhang, Y.; Li, M.; Lang, X.-Y.; Zhang, Y.; Liu, Z. Dendritic, transferable, strictly monolayer MoS_2 flakes synthesized on $SrTiO_3$ single crystals for efficient electrocatalytic applications. *ACS Nano* **2014**, *8*, 8617-8624.
(62) Zhang, Y.; Ji, Q.; Wen, J.; Li, J.; Li, C.; Shi, J.; Zhou, X.; Shi, K.; Chen, H.; Li, Y.; Deng, S.; Xu, N.; Liu, Z.; Zhang, Y. Monolayer MoS_2 dendrites on a symmetry-disparate $SrTiO_3$ (001) substrate: formation mechanism and interface interaction. *Adv. Funct. Mater.* **2016**, *26*, 3299-3305.
(63) Li, J.; Chen, M.; Zhang, C.; Dong, H.; Lin, W.; Zhuang, P.; Wen, Y.; Tian, B.; Cai, W.; Zhang, X. Fractal-theory-based control of the shape and quality of CVD-grown 2D materials. *Adv. Mater.* **2019**, *31*, e1902431.
(64) Cong, C.; Shang, J.; Wu, X.; Cao, B.; Peimyoo, N.; Qiu, C.; Sun, L.; Yu, T. Synthesis and optical properties of large-area single-crystalline 2D semiconductor WS_2 monolayer from chemical vapor deposition. *Adv. Opt. Mater.* **2014**, *2*, 131-136.
(65) Cui, F.; Li, X.; Feng, Q.; Yin, J.; Zhou, L.; Liu, D.; Liu, K.; He, X.; Liang, X.; Liu, S.; Lei, Z.; Liu, Z.; Peng, H.; Zhang, J.; Kong, J.; Xu, H. Epitaxial growth of large-area and highly crystalline anisotropic $ReSe_2$ atomic layer. *Nano Res.* **2017**, *10*, 2732-2742.
(66) Hao, Y.; Bharathi, M. S.; Wang, L.; Liu, Y.; Chen, H.; Nie, S.; Wang, X.; Chou, H.; Tan,

C.; Fallahazad, B.; Ramanarayan, H.; Magnuson, C. W.; Tutuc, E.; Yakobson, B. I.; McCarty, K. F.; Zhang, Y. W.; Kim, P.; Hone, J.; Colombo, L.; Ruoff, R. S. The role of surface oxygen in the growth of large single-crystal graphene on copper. *Science* **2013**, *342*, 720-723.
(67) Wang, J.; Cai, X.; Shi, R.; Wu, Z.; Wang, W.; Long, G.; Tang, Y.; Cai, N.; Ouyang, W.; Geng, P.; Chandrashekar, B. N.; Amini, A.; Wang, N.; Cheng, C. Twin defect derived growth of atomically thin MoS_2 dendrites. *ACS Nano* **2018**, *12*, 635-643.
(68) López-Sánchez, J.; Muñoz-Noval, A.; Serrano, A.; Abuín, M.; de la Figuera, J.; Marco, J. F.; Pérez, L.; Carmona, N.; Rodríguez de la Fuente, O. Growth, structure and magnetism of ε-Fe_2O_3 in nanoparticle form. *RSC Adv.* **2016**, *6*, 46380-46387.
(69) Ahmmad, B.; Leonard, K.; Shariful Islam, M.; Kurawaki, J.; Muruganandham, M.; Ohkubo, T.; Kuroda, Y. Green synthesis of mesoporous hematite (α-Fe_2O_3) nanoparticles and their photocatalytic activity. *Adv. Powder. Technol.* **2013**, *24*, 160-167.
(70) Qu, J.; Yu, Y.; Cao, C. Y.; Song, W. G. α-Fe_2O_3 nanodisks: layered structure, growth mechanism, and enhanced photocatalytic property. *Chemistry* **2013**, *19*, 11172-11177.
(71) Faure, B.; Wetterskog, E.; Gunnarsson, K.; Josten, E.; Hermann, R. P.; Bruckel, T.; Andreasen, J. W.; Meneau, F.; Meyer, M.; Lyubartsev, A.; Bergstrom, L.; Salazar-Alvarez, G.; Svedlindh, P. 2D to 3D crossover of the magnetic properties in ordered arrays of iron oxide nanocrystals. *Nanoscale* **2013**, *5*, 953-960.
(72) Ziolo, R. F.; Giannelis, E. P.; Weinstein, B. A.; Horo, M. P.; Ganguly, B. N.; Mehrotra, V.; Russell, M. W.; Huffman, D. R. Matrix-mediated synthesis of nanocrystalline γ-Fe_2O_3: A new optically transparent magnetic material. *Science* **1992**, *257*, 219-223.
(73) Schabes, M. E.; Bertram, H. N. Ferromagnetic switching in elongated γ - Fe_2O_3 particles. *J. Appl. Phys.* **1988**, *64*, 5832-5834.
(74) Wu, J.; Mao, S.; Ye, Z. G.; Xie, Z.; Zheng, L. Room-temperature weak ferromagnetism induced by point defects in α-Fe_2O_3. *ACS Appl. Mater. Inter.* **2010**, *2*, 1561-1564.
(75) Puthirath Balan, A.; Radhakrishnan, S.; Woellner, C. F.; Sinha, S. K.; Deng, L.; Reyes, C. d. l.; Rao, B. M.; Paulose, M.; Neupane, R.; Apte, A.; Kochat, V.; Vajtai, R.; Harutyunyan, A. R.; Chu, C.-W.; Costin, G.; Galvao, D. S.; Martí, A. A.; van Aken, P. A.; Varghese, O. K.; Tiwary, C. S.; Malie Madom Ramaswamy Iyer, A.; Ajayan, P. M. Exfoliation of a non-van der Waals material from iron ore hematite. *Nat. Nanotechnol.* **2018**, *13*, 602-609.
(76) Liu, R.; Jiang, Y.; Lu, Q.; Du, W.; Gao, F. Al^{3+}-controlled synthesis and magnetic property of α-Fe_2O_3 nanoplates. *CrystEngComm* **2013**, *15*, 443-446.

Figure 1

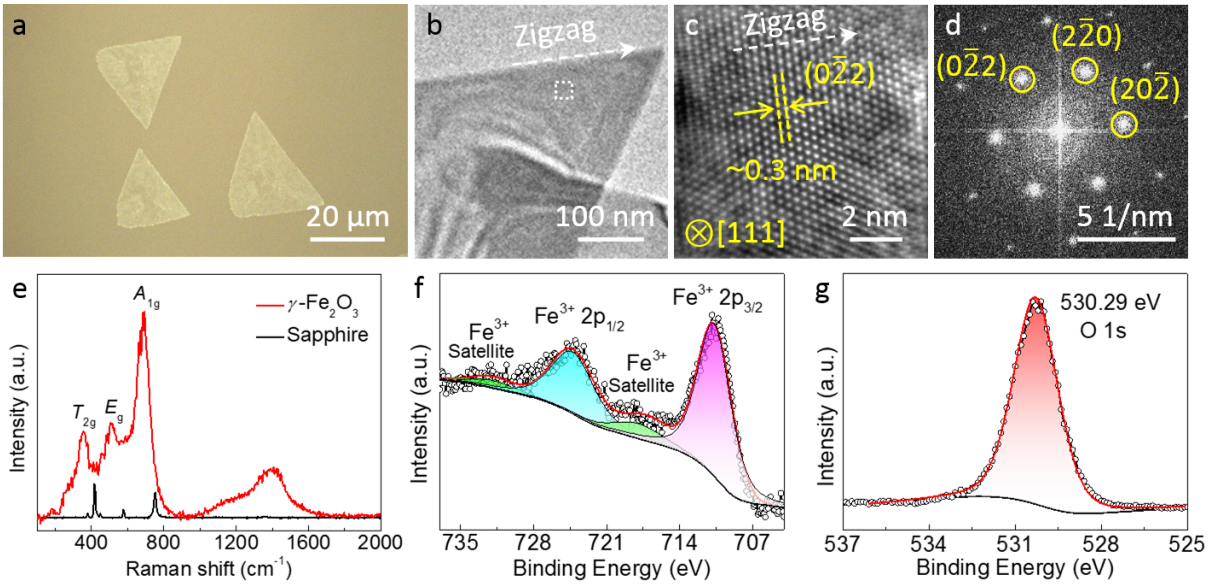

Figure 1 Characterization of γ-Fe_2O_3 nanoflakes. (a) Optical image of three triangular γ-Fe_2O_3 nanoflakes grown on sapphire substrate. (b) TEM image of a transferred γ-Fe_2O_3 nanoflake. (c) High-resolution TEM image taken from the square-marked area in (b), which is projected along [111] zone axis of the γ-Fe_2O_3 nanoflake. The white arrow indicates the zigzag direction, as also marked in a white arrow in (b). The (0$\bar{2}$2) plane spacing is ~0.3 nm. (d) Corresponding FFT patterns of the HRTEM image in (c), which displays only one set of sixfold symmetry spots. (e) Raman spectra of the γ-Fe_2O_3 nanoflake and sapphire. The red curve contains five main peaks at ~356, 512, 650–720, 1200, and 1400 cm^{-1}. (f,g) High-resolution XPS spectra of the Fe 2p (f) and O 1s (g) region.

Figure 2

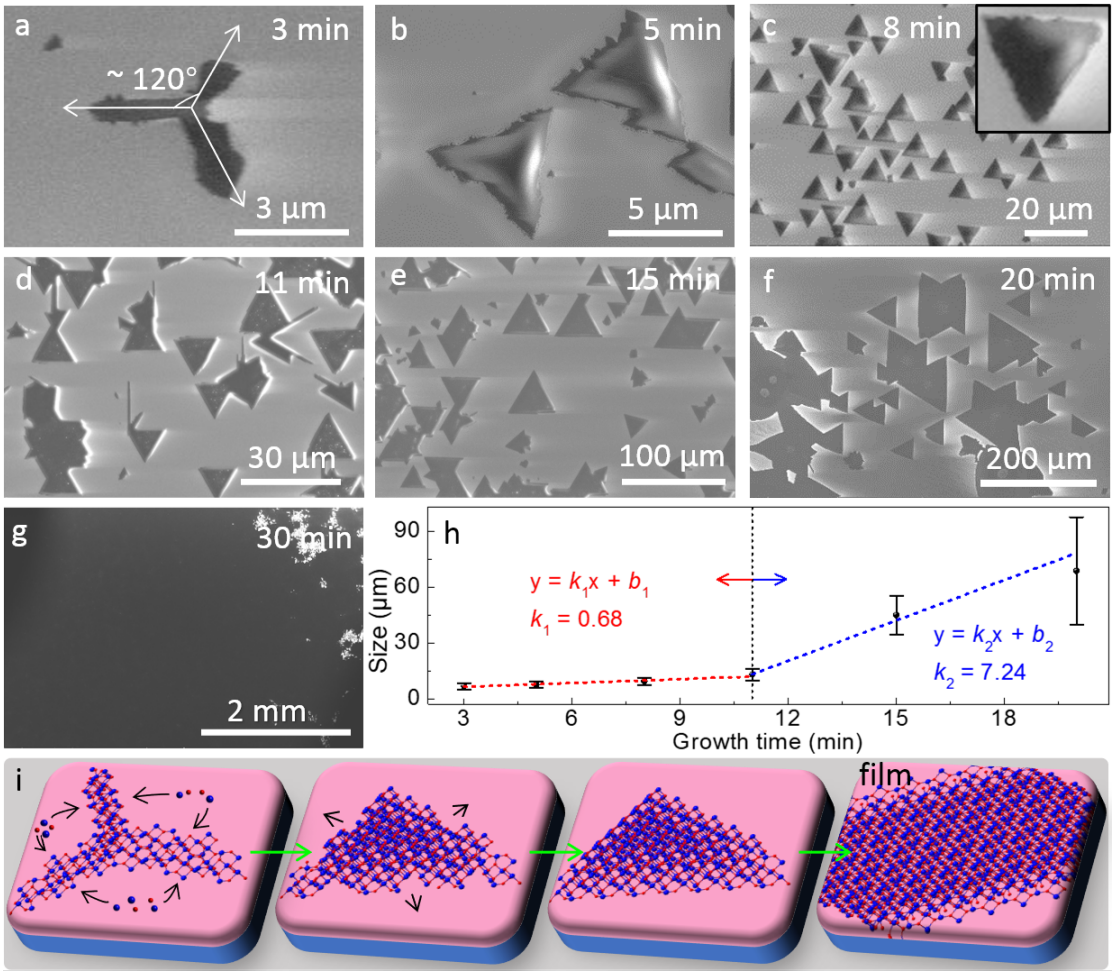

Figure 2 Characterization of the growth process of triangular γ-Fe_2O_3 nanoflakes. (a–g) SEM images of the as-grown γ-Fe_2O_3 nanoflakes with the increase of growth time (3, 5, 8, 11, 15, 20, and 30 min), revealing the effect of growth time on crystal shape and size. (h) Size of γ-Fe_2O_3 nanoflakes as a function of growth time, showing linear relationships between size and growth time at different stages. The slopes of the initial and rapid growth stages are estimated to be 0.68 and 7.24, respectively. (i) Schematic of the growth process of γ-Fe_2O_3, ranging from dendrite formation, filling defects, growth, to formation of film.

Figure 3

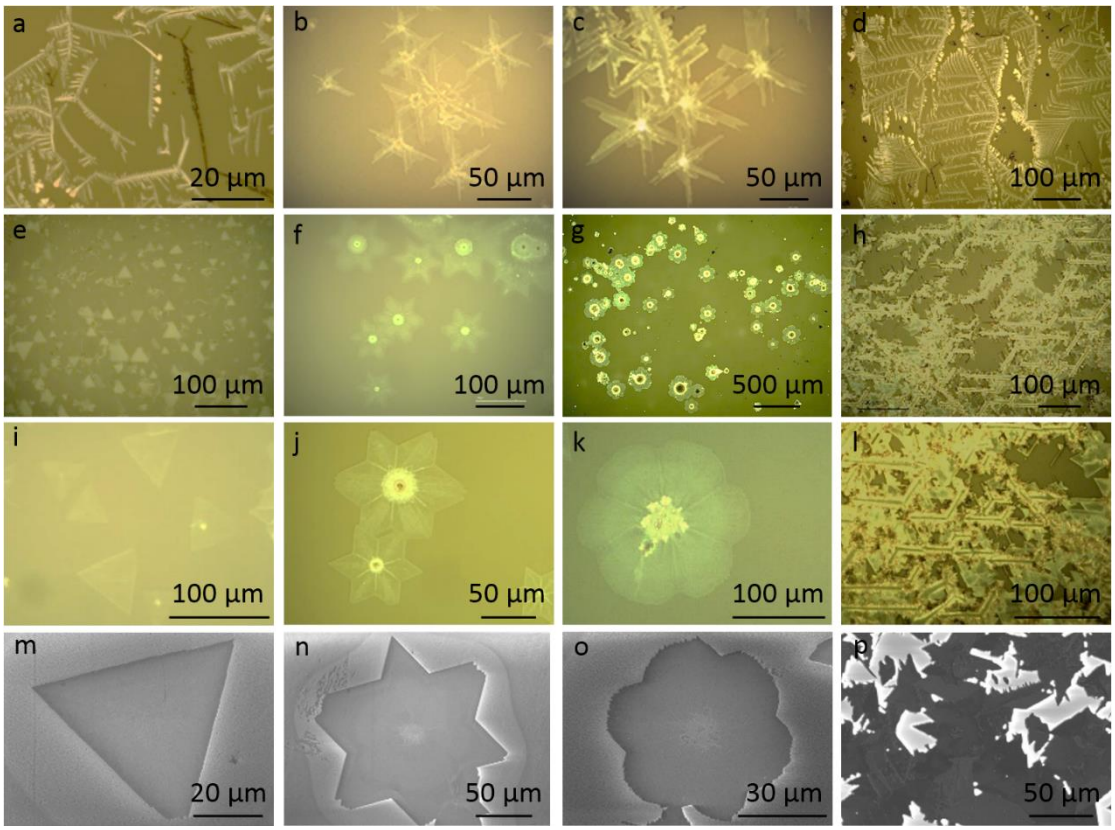

Figure 3 Characterization of the stage-by-stage formation of the γ-Fe_2O_3 nanoflakes grown at different temperatures (~930°C, 980°C, 1030°C, and 1080°C), uncovering five growth models. (a–d) OM images of the as-grown triangular (a), stellated (b), petaloid (c), and dendritic (d) γ-Fe_2O_3 nanoflakes at the initial growth stage. (e–h) OM images of the as-grown triangular (e), stellated (f), petaloid (g), and dendritic (h) γ-Fe_2O_3 nanoflakes at the mature growth stage. (i–l) High-magnification OM images corresponding to the low-magnification OM images in (e–h). (m–p) SEM images of triangular (m), stellated (n), petaloid (o), and dendritic (p) γ-Fe_2O_3 nanoflakes.

Figure 4

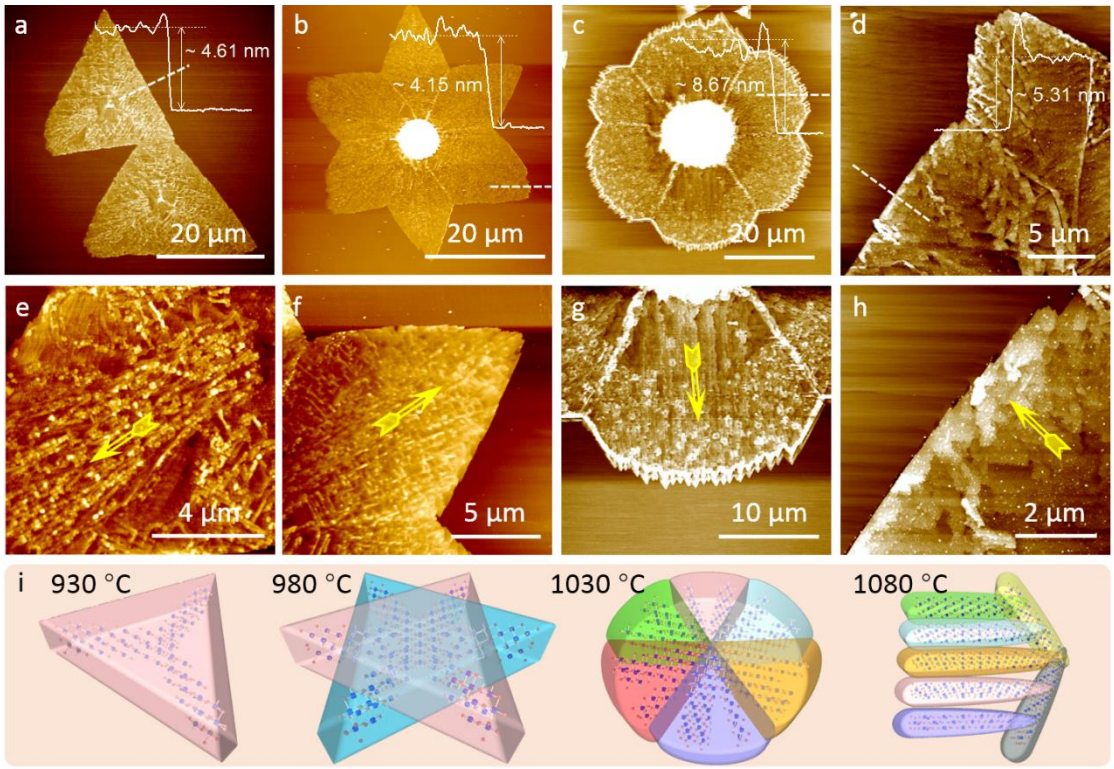

Figure 4 Characterization of surface profile. (a–d) AFM images of triangular (a), stellated (b), petaloid (c), and dendritic (d) γ-Fe_2O_3 nanoflakes. The insets show the corresponding profile lines of the γ-Fe_2O_3 nanoflakes, indicating that the thickness of the nanoflakes in (a) to (d) is about 4.61, 4.15, 8.67, and 5.31 nm, respecticely. (e–h) High-magnification AFM images corresponding to the low-magnification AFM images in (a–d). The yellow arrows delineate the growth pathways of γ-Fe_2O_3 nanoflakes. (i) Sketch of the triangular, stellated, petaloid, and dendritic γ-Fe_2O_3 nanoflakes synthesized at 930°C, 980°C, 1030°C, and 1080°C.

Figure 5

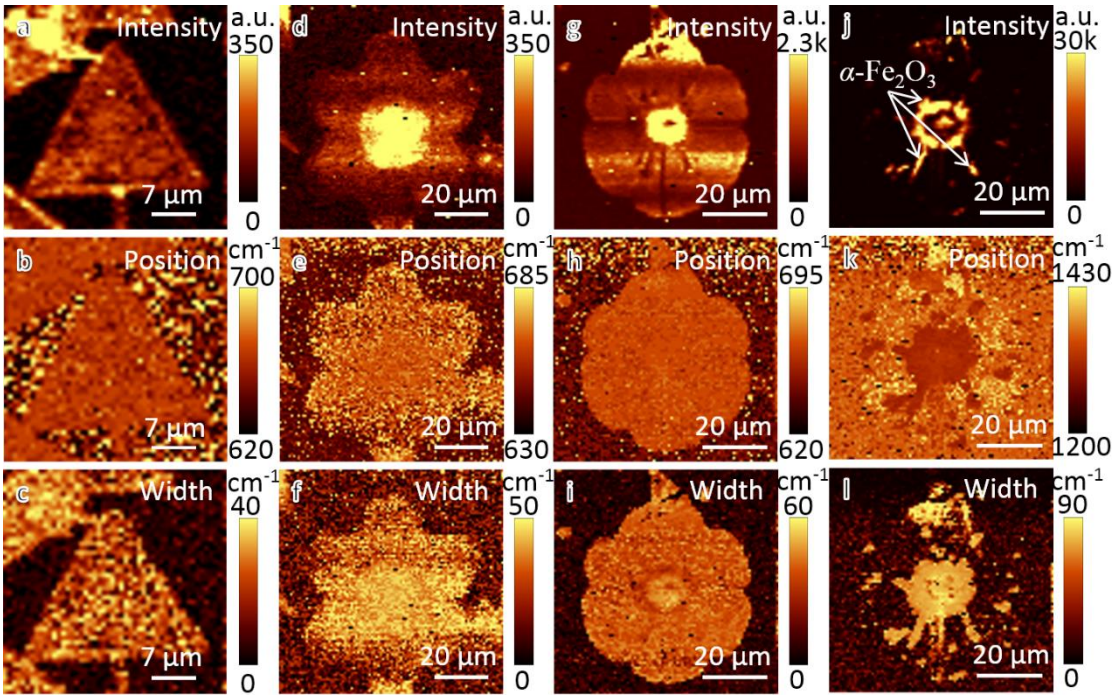

Figure 5 Raman characterization of the triangular, stellated, petaloid, and dendritic γ-Fe_2O_3 nanoflakes. (a–c) Raman A_{1g} mode mapping images of intensity (a), position (b), and width (c) for a triangular γ-Fe_2O_3 nanoflake. (d–f) Raman A_{1g} mode mapping images of intensity (d), position (e), and width (f) for a stellated γ-Fe_2O_3 nanoflake. (g–i) Raman A_{1g} mode mapping images of intensity (g), position (h), and width (i) for a petaloid γ-Fe_2O_3 nanoflake. (j–l) Intensity (j), position (k), and width (l) mapping images of a Raman peak at ~1315 cm^{-1} for the petaloid γ-Fe_2O_3 nanoflake in (g–i).

Figure 6

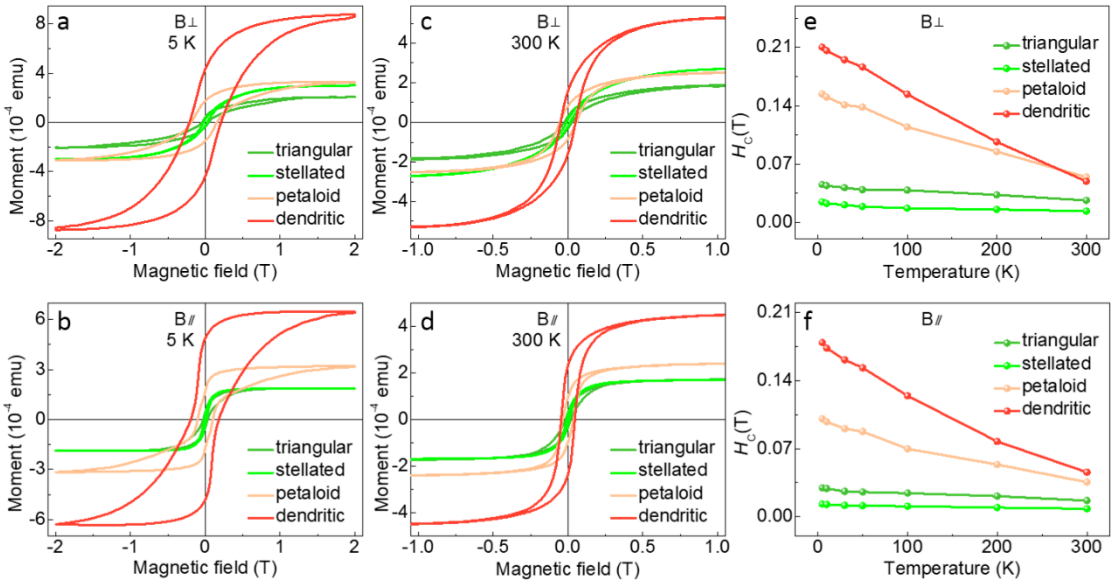

Figure 6 Characterization of ferromagnetic performance of γ-Fe_2O_3 nanoflakes. (a,b) Magnetic hysteresis (*M*-*H*) loops of the triangular, stellated, petaloid, and dendritic γ-Fe_2O_3 nanoflakes measured under vertical (a) and parallel (b) fields at 5 K. (c,d) *M*-*H* loops of triangular, stellated, petaloid, and dendritic γ-Fe_2O_3 nanoflakes measured under vertical (c) and parallel (d) fields at 300 K. The diamagnetic contribution from α-Al_2O_3 substrate is subtracted. (e,f) Temperature-dependent coercive force (H_C) for γ-Fe_2O_3 nanoflakes measured under vertical (e) and parallel (f) magnetic fields.

Figure 7

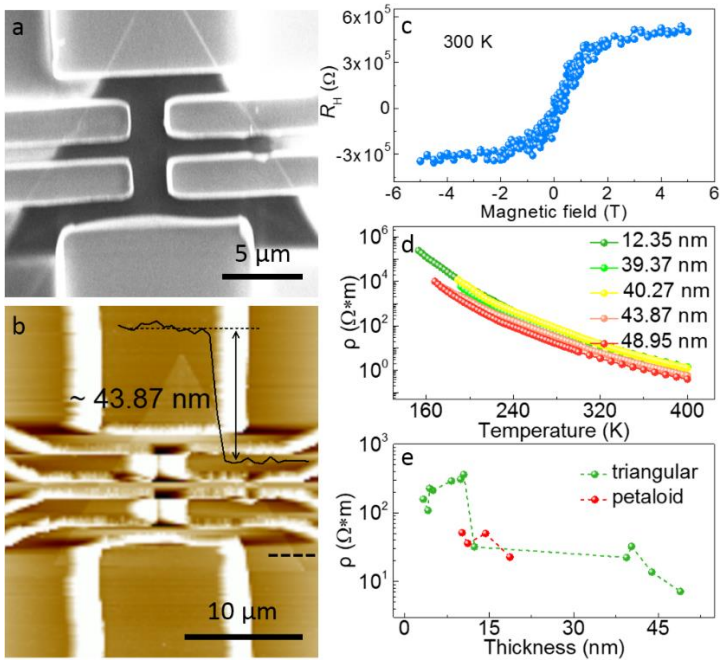

Figure 7 Magnetic and electrical transport measurements of γ-Fe_2O_3 nanoflakes. (a,b) SEM (a) and AFM (b) images of a triangular γ-Fe_2O_3 Hall device. The inset shows the height profile line of the Hall device. (c) Hall resistance (R_H) as a function of magnetic field measured at 300 K for the Hall device shown in (a). (d) Temperature-dependent electrical transport measurement of the electrical resistivity (ρ) as thickness varies (12.35, 39.37, 40.27, 43.87, and 48.95 nm). (e) Thickness-dependent ρ for triangular and petaloid γ-Fe_2O_3 nanoflakes.